Hidden soils and their carbon stocks at high-elevation in the European Alps (North-West Italy)

(Article begins on next page)

29 November 2024

Hidden soils and their carbon stocks at high-elevation in the European Alps (North-West Italy)

Emanuele Pintaldi[1], Michele E. D'Amico[1*], Nicola Colombo[1,2,3], Chiara Colombero[4], Luigi Sambuelli[4], Claudio De Regibus[4], Diego Franco[4], Luigi Perotti[3], Luca Paro[5], Michele Freppaz[1,2]

[1]University of Turin, Department of Agricultural, Forest and Food Sciences (DISAFA), Largo Braccini, 2, 10095 Grugliasco (TO), Italy.

[2]University of Turin, Research Center on Natural Risk in Mountain and Hilly Environments (NatRisk), Largo Braccini, 2, 10095 Grugliasco (TO), Italy.

[3]University of Turin, Department of Earth Sciences (DST), Via Valperga Caluso, 35, 10125 Turin, Italy.

[4]Politecnico di Torino, Department of Environment, Land and Infrastructure Engineering (DIATI), Corso Duca degli Abruzzi, 24, 10129 Turin, Italy.

[5]Regional Agency for Environmental Protection (Agenzia Regionale per la Protezione Ambientale - ARPA) of Piedmont, Via Pio VII, 9, 10135 Turin, Italy.

Abstract

Alpine soils store large quantities of total organic carbon (TOC). Given their high sensitivity to climate change, they may release large amounts of CO_2 in a warming climate scenario. Thus, it is important to know their C stocks in order to estimate its possible release. While C stocks of forest, dwarf shrub and alpine grassland soils are well documented, little is known about soils and C stocks in high-elevated periglacial environments dominated by frost-driven processes. The object of this study is the periglacial environment of the Stolenberg Plateau (LTER site Istituto Mosso, 3030 m a.s.l.), at the foot of the Monte Rosa Massif (NW Italian Alps). The plateau is mostly covered by a

thick stony layer, organized in periglacial blockfields and blockstreams. The plant cover reaches only 3-5%. During the construction of a chair lift, open trenches revealed, unexpectedly, well-developed soils under the active periglacial stone cover. In particular, thick (30-65 cm) and dark TOC-rich A horizons were observed. Below these Umbric horizons, Cambic Bw ones were developed but discontinuous. Despite the lack of vegetation, C stocks were remarkably high (up to ~5 kg m^{-2}), comparable to vegetated soils at lower elevation. Non-invasive geophysical methods revealed that these hidden soils were widespread on the plateau under the stony cover, with a mean thickness of around 50 cm. These TOC-rich soils, without vegetation and covered by periglacial landforms, represent a unique pedoenvironment suggesting new perspectives on the actual C-stocks at high-elevation sites, which are probably underestimated.

Keywords

Soil organic matter; Periglacial; Blockstream/Blockfield; Skeletic Umbrisol (Arenic, Turbic)

1 Introduction

Soil Organic Matter (SOM) stored in alpine soils (i.e. soils developed above the timberline, in alpine tundra and alpine desert, etc.) represents a considerable part of the global C cycle (e.g. Bockheim and Munroe, 2014), acting as a sink for carbon dioxide and having therefore a great potential to sequestrate this from the atmosphere (Bojko and Kabala, 2017). Alpine soils, especially those covered by vegetation and/or affected by permafrost, store large quantities of organic carbon (e.g. Celi et al., 2010; Bockheim and Munroe, 2014). However, given the high sensitivity of soils to climate change (Hagedorn et al., 2010a; Stanchi et al., 2015), they may release large amounts of carbon dioxide in a warming climate scenario (e.g. Hagedorn et al., 2010b; Schuur et al., 2013; Knowles et al., 2019). Generally, at high elevations in the European Alps, soils are mainly classified as Regosols, Cambisols, or Podzols (e.g. Egli et al., 2006; Zollinger et al., 2013; D'Amico et al.,

2020), often showing evidences of cryoturbation. In particular, high-elevation soils (i.e. above the alpine treeline) are affected by frost-action processes (e.g. frost-shattering, frost sorting, frost heave, solifluction etc.) (Karte, 1983), induced by seasonal frost penetration and/or permafrost (Van Vliet-Lanoë, 2014), leading to the formation of patterned ground, typical of periglacial environments (e.g. tilting of stones, blockstreams, blockfields, wedges, etc.) (e.g. Goodfellow, 2007; D'Amico et al., 2019). As these processes are mostly driven by temperature, active patterned ground is sensitive to climate warming, which can induce several effects such as permafrost degradation (e.g. Biskaborn et al., 2019; Mollaret et al., 2019), expansion of plant cover (e.g. Gerdol and Smiraglia, 1990), transition from pioneer species communities towards more acidophilous grassland (D'Amico et al., 2015), and increased SOM decomposition (e.g. Arteaga et al., 2008; Hagedorn et al., 2010a).

While the carbon stocks of forest and alpine grassland soils are well documented by several studies (e.g. Leifeld et al., 2009; Zollinger et al., 2013; Bockheim and Munroe, 2014), very little is known about carbon stocks in high-elevated periglacial environments, especially in the European Alps. This is probably due to different reasons, such as: 1) these soils are located in very unfavorable positions at high elevation and they are often difficult to reach, requiring specific technical equipment; 2) generally, these high-elevation areas are not covered by vegetation, therefore, as plants are the primary carbon source, these soils received less interest since they are not considered a relevant carbon sink compared to other soils; 3) high-elevation soils are often in periglacial environments, which are characterized by cryoturbation processes (induced by low temperatures and/or permafrost) that allow the formation of patterned ground and solifluction, which create an extreme spatial variability (D'Amico et al., 2015). They are frequently covered by coarse debris which makes it difficult to recognize them as soils and perform in-depth pedological investigations using manual devices.

In order to deepen the knowledge on these periglacial stone-covered environments, geophysical methods can be used thanks to their capability to map soil thickness even in areas with undulating topography, complex spatial distribution and non-homogeneous or anisotropic properties of the

investigated materials. Among the available geophysical methods, Electrical Resistivity Tomography (ERT) allows investigating contrasts in electrical properties between the soil (loose, porous, prone to water retention and possibly rich in organic matter) and massive bedrock or coarse deposits. The same contrast in physical properties, together with differences in layering and other internal structures, can be imaged using Ground Penetrating Radar (GPR) profiling. ERT and GPR are widely used to support pedological surveys for soil characterization, mapping of the presence, depth and lateral variability of soil horizons, agricultural purposes and contamination analyses from low to mid latitudes and elevations (e.g. Samouelian et al., 2005; Allred et al., 2008; Doolittle and Butnor, 2009; Andre et al., 2012; Nováková et al., 2013). By contrast, only few applications of geophysical prospections for the study of high-elevation soils are reported in the literature (e.g. Leopold et al., 2010; Pellet et al., 2016; Mollaret et al., 2019). In periglacial environments, these techniques are mainly used for permafrost characterization, hydrogeological processes and loose material-bedrock interface recognition (Moorman et al., 2003; Otto and Sass, 2006; Kneisel et al., 2008; McClymont et al., 2010; Léger et al., 2017).

The research was performed in the severe periglacial environment of the Stolenberg Plateau on the southern slope of Monte Rosa Massif (NW Italian Alps) where, in 2017, unexpected well-developed soils within blockfields/blockstreams were found. Considering the impossibility to deepen the investigation using manual devices and machinery, and the necessity to detect the distribution of these hidden soils, non-invasive geophysical methods were applied in September 2019.

In this context, this work aims at: 1) describing and classifying the hidden soils, 2) determining their carbon stock, and 3) investigating their local distribution and thickness, and potential relationships with permafrost presence/distribution.

2 Materials and methods

2.1 Study Area

The work was carried out in the periglacial environment of the Stolenberg Plateau, a 13,500 m^2 almost flat area located at 3030 m a.s.l., at the boundary between Valle d'Aosta and Piemonte regions (Fig. 1a), at the foot of the southern slope of Monte Rosa (4634 m) (NW Italian Alps). The study site represents the summit portion of the Long Term Ecological Research (LTER) site Angelo Mosso Scientific Institute (LTER-Italia IT19-001-T), belonging to the LTER-Italy network. The study area is also a Site of Community Importance and a Special Protection Area (SCI/SPA IT1204220 "Ambienti glaciali del gruppo del Monte Rosa") (European Commission, 1992) belonging to the Natura 2000 network.

From 2007 to 2018, the area had a mean annual air temperature of –2.2 °C, a mean cumulative annual snowfall of 818 cm, and a mean annual liquid precipitation of ca. 400 mm. Snow cover lasts for at least 8 months, reaching a maximum thickness of ca. 350 cm (Freppaz et al., 2019). In the LTER-Italia IT19-001-T site, although at lower elevation and with alpine vegetation cover (snowbed and grassland communities), soils were classified as Skeletic Dystric Regosol, Skeletic Umbrisol, and Skeletic Dystric Cambisol (IUSS Working Group WRB, 2015) (Magnani et al., 2017). Permafrost was detected at depths higher than 3-4 m on the nearby Corno del Camoscio (3024 m a.s.l.) (Colombo et al., 2019). On the plateau, the slope steepness is below 10%, with large flat portions in the central and eastern parts. The area shows typical features of periglacial environments, characterized by active periglacial landforms. In particular, the plateau is covered by a thick layer of stones with variable size (from decimeter to meter), well organized in blockfields, blockstreams/sorted stripes, gelifluction lobes, tilted stones and weakly developed sorted circles (Fig. 1b). In particular, blockstreams partly rearranged into sorted stripes are visible on sloping surfaces, while blockfields, partly rearranged into patterned ground and rich in standing stones, dominate the flatter surfaces. The activity of the periglacial processes is evidenced by the absence of lichens from most stones (Ballantyne and Matthews, 1982). The parent material is composed of gneiss and mica-schists (Monte Rosa nappe, Pennidic basement) and metabasites (Zermatt-Saas unit) (Mattirolo et al., 1951). No traces of glacial till are observed, as all blocks seem autochthonous

129 (Ballantyne, 2010; Goodfellow, 2007); the best developed blockstreams are located around rock

130 outcrops, and are clearly derived by their cryofracturation. The glacial history of the plateau is

131 currently unknown.

132 The vegetation cover, which is extremely scarce and confined to small patches reaching no more

133 than 5% of the plateau areal extension, is composed mainly of alpine and nival species such as

134 *Silene acaulis, Carex curvula, Salix herbacea* in the vegetated patches, while *Festuca halleri, Poa*

135 *alpina, Ranunculus glacialis, Leuchantemopsis alpina, Cerastium uniflorum* and a few other

136 pioneer species grow also in the stone-covered area, with extremely low cover values. A higher

137 vegetation cover characterizes a small area in the northern side, close to the edge of the cliff, on

138 slightly more weatherable amphibolites.

139

2.2 Soil survey, sampling and analysis

141 In 2017, during the operational activities for the construction of a new chair lift, the largest part of

142 the plateau was delimited in order to protect the natural environment (Directive, 1992) and the

143 periglacial features against the excavation operations. However, three trenches were opened (2 to 10

144 m long, to a depth of around 1.2 m) in the construction area, revealing unexpected, well-developed

145 soils under the stony cover. This finding was possible only thanks to the machinery employed,

146 whose utilization was exceptionally allowed for the construction of the chair lift station.

147 Field description of soil transects was performed according to FAO (2006), while soil classification

148 was done according to WRB classification system (IUSS Working Group WRB, 2015). The three

149 trenches (soil profiles) were described and sampled (Fig. 1a). Each profile was subdivided into

150 sectors characterized by a similar sequence of horizons. Overall, 27 soil samples were collected

151 from all genetic horizons in the profiles; at least one sample per genetic horizon was sampled in

152 each sector (ca. 300-500 g per sample). The samples were air-dried, sieved to 2 mm and analyzed

153 following the standard methods reported by Van Reeuwijk (2002). The pH was measured in soil-

154 water suspension (soil:water = 1:2.5). The particle-size analysis was performed by the pipette

method after organic matter destruction with H_2O_2 followed by dispersion with Na-hexametaphosphate. Total carbon (corresponding to total organic carbon-TOC due to the absence of carbonates) and nitrogen (TN) concentrations, were measured by dry combustion with an elemental analyzer (CE Instruments NA2100, Rodano, Italy).

The soil organic carbon stock (C-STOCK$_{tot}$ kg m^{-2}) of the profiles was calculated for sectors in which the horizons sequence was similar, according to the following equation adapted from Batjes (1996):

$$C - STOCKtot = \sum_{i=1}^{n} \frac{TOC*BD*TH*VF}{1000} \tag{1}$$

where *n* is the number of soil horizons of each sector, TOC is the soil organic carbon concentration (g kg^{-1}) of the mineral horizons, BD is the Bulk Density (kg m^{-3}) based on mean Bulk Density values of high-elevation soils (D'Amico et al., still unpublished) measured according to Boone et al. (1999), TH is the horizon thickness (m), VF is the volume of fine earth excluding the coarse mineral fraction (> 2 mm, visually estimated in the field (%) for each horizons), calculated as [1 − (% rock volume/100)], 1000 is the unit correction factor.

In order to support the interpretation of the geophysical measurements, the clay minerals were analyzed using a Philips PW1710 X-ray diffractometer (40kV and 20 mA, CoKα radiation, graphite monochromator). The Mg saturated clay fraction (< 2 µm) was separated by sedimentation, flocculated with MgCl$_2$, washed until free of Cl$^-$, and freeze-dried. Scans were made from 3 to 35 º2θ at a speed of 1 º2θ min^{-1}, on air dried, ethylene glycol solvated, and heated (350° and 550 °C) oriented mounts. A semi-quantitative evaluation of mineral abundance was performed using the Mineral Intensity Factors method (Islam and Lotse, 1986), which considers peak areas. For the calculation, the background was subtracted and the peak positions, intensities and areas were calculated using the PowderX software (Dong, 1999).

2.3 Geophysical investigation

Six 48-electrode Electrical Resistivity Tomography (ERT) profiles were acquired (Fig. 1a). Five of them had an inter-electrode spacing of 0.30 m, for a total length of 14.1 m. One longer profile (ERT 3 in Fig. 1a) was acquired with a spacing of 2 m between the electrodes, for a total length of 94 m. With the short profiles we aimed at the detection and lateral imaging at shallow depths of the buried soils with high-resolution, while the longer line was designed for a deeper general low-resolution characterization of the bedrock conditions below the soil horizons. To constrain data interpretation, reference values for the soil electrical resistivity were derived from the statistical analysis of measurements carried out in an uncovered soil outcrop (approximately 1.5 x 0.3 m) with a single quadrupole (0.25-, 0.30- and 0.40-m electrode spacing, eight array configurations of current and potential electrode positions).

ERT electrodes were georeferenced using a Garmin GPS 60 system to overlay the position of each survey line on a high-resolution digital surface model (DSM) of the plateau and later account for the significant topographic variations in the inversion of the longest ERT line. Digital vertical and slantwise photos obtained from an Unmanned Aerial Vehicle (UAV) survey were processed with structure from motion and multi-view-stereo algorithms to produce a high-resolution DSM (10 cm / pixel ground resolution) of the investigated area (e.g. Smith et al., 2015; Carrivick et al., 2016, Alberto et al., 2018) (Supplementary Material, SM1).

Ten ground penetrating radar (GPR) profiles (Fig. 1a) were complementary acquired with a 500-MHz antenna controlled by an IDS K2 digital acquisition unit. GPR traces were acquired for a total time of 100 ns and 512 samples per trace. Ublox EVK-5T GPS was used to track each survey position. The average distance between subsequent traces resulted in 0.025 m along each line.

Local rare diffraction hyperbola in the processed radargrams were fitted with a velocity of 0.1 m/ns. To apply this value for time-to-depth conversion, the medium velocity (v) was additionally estimated by the Complex Refractive Index Method (CRIM, Birchak et al., 1974; Wharton et al., 1980), following:

$$\sqrt{\varepsilon_S} = (1 - \varphi) \sqrt{\varepsilon_m} + \varphi\, S\, \sqrt{\varepsilon_w} + \varphi\, (1 - S)\, \sqrt{\varepsilon_a} \qquad\qquad (2)$$

206 and

207 $$v = \frac{c}{\sqrt{\varepsilon_S}} \qquad\qquad\qquad\qquad\qquad\qquad (3)$$

208 where ε_S, ε_m, ε_w and ε_a are the relative dielectric permittivities of soil (solid matrix + pore space),

209 solid matrix, pore water and air respectively, φ is the soil porosity, S is the degree of water

210 saturation and c is the electromagnetic wave velocity in vacuum ($3 \cdot 10^8$ m/s). In Equation 2, $\varepsilon_a = 1$,

211 $\varepsilon_w = 77.8$ (from GPR measurements on the water of a nearby pond; Colombo et al., 2018) and $\varepsilon_m = 7$

212 (from average reference values of similar loamy sandy soils, e.g. Daniels, 2004). Soil porosity φ

213 was indirectly estimated from density measurements in the range 0.5 to 0.6. Moist (unsaturated)

214 conditions were present on site during GPR acquisitions. A variable S, between 0.2 and 0.4, was

215 consequently considered in the computation. Using these parameters, average $\varepsilon_S = 9.3$ and $v = 0.10$

216 m/ns were obtained for time-to-depth conversion. The approximate wavelength of a 500-MHz GPR

217 signal in this material is consequently 0.2 m, meaning approximately 0.1 m of vertical resolution

218 (half wavelength) in the investigated medium.

219 Additional details on ERT and GPR processing are given in Supplementary Material SM2.

220

221 2.4. Bottom temperature of snow cover and ground temperature

222 To investigate the ground surface thermal conditions in the investigated area, the bottom

223 temperature of the snow cover (BTS, e.g. Hoelzle, 1992) measurements were performed in 2014,

224 2015, and 2019. To acquire BTS data, a thermometer Delta Ohm RTD HD 2307.0 (accuracy ±0.05

225 °C, resolution 0.1 °C), equipped with a probe Pt100 TP474C.0, was installed on a stainless steel

226 probe. The location of each sample point was recorded with a handheld Global Positioning System

227 (GPS) ("Aventura" TwoNav vs. 2.6.2). The measurements were performed during the late winter

228 (March/April), when a sufficient snow cover was established since at least one month, before the

229 onset of snow melt. Since a minimum snow thickness of 80 cm is necessary to provide a sufficient

insulation against air temperature variations, measurements were made only where this threshold was found, obtaining about 260 measurements.

Ground temperature (GT) data from a 5-m deep borehole managed by Arpa Piemonte in the north-eastern side of the plateau were also used to analyse the ground thermal conditions. Daily data from 04 November 2017 to 29 July 2019 were analysed; no data gaps were present in the series.

3 Results

3.1. Soil profiles characteristics

The stony/blocky layer (blockfields and blockstreams, respectively on flat surfaces or on gentle slopes) was 10-60 cm thick, and it was usually well graded with depth, with the coarsest stones on the surface and fine ones at the bottom, associated with A1 horizons, as typically observed in blockfields and blockstreams (Wilson, 2013). Below the stone layer, the profiles were characterized by thick (between 30 and 65 cm) and continuous, dark A and A@ horizons with subangular-blocky, platy or granular structure (Table 1, Figs. 2, 3 and 4). These horizons were characterized by few living or dead roots and very few, extremely weak, isolated, biogenic fine granular aggregates. They were classified as Umbric horizons according to WRB (IUSS Working Group WRB, 2015). In fact, the diagnostic criteria for Umbric horizons, calculated in the top 20 cm, are dark colors (moist chroma and value ≤ 3), darker colors than the horizons underlying it or the parent material, soft or friable consistence and not massive structure, $\geq 0.6\%$ TOC, pH < 5.5 or base status $< 50\%$. Below the Umbric horizons, Cambic Bw ones were often developed although discontinuous, characterized by brown color and well-developed subangular-blocky structure (Table 1, Figs. 2, 3 and 4). Stones were quite scarce, particularly in A horizons, evidencing frost sorting and cryoexpulsion. The stones were moderately weathered and were quite easily broken with a spade, particularly in Bw horizons, while they were weakly weathered in the surface layer. Cryoturbation features, such as inclusions of surface A materials at depth (horizons n. 7 in Fig. 3) as well as convolutions and block

displacement above wedges, were often observed within the profiles. In profile 3, blocks shown as "a" in Fig. 2 were dislocated and raised by freeze-thaw processes from the rock layer evidenced by letters "b" and "c", above a deep fracture (wedge). Thick, dense silt caps were also observed on the upper faces of stone fragments. Below the Bw, BC and CB horizons, the highly fractured bedrock was always observed. The soils were classified as Skeletic Umbrisol (Arenic, Turbic), according to IUSS Working Group WRB (2015).

3.2 Soils physical and chemical properties

The soil texture of all horizons was generally loamy sand or sandy loam, with a substantial prevalence of sand (77% on average) compared to silt (20%) and clay (3%) fractions (Tab. 1). The clay fraction was composed of ca. 60% quartz, 20% mica/illite, 10% chlorite, 10% plagioclase and other minerals in traces (not shown), reflecting a similar mineralogy as the parent material. pH values were extremely to moderately acidic, ranging between 4.3 and 5.9. TOC content spanned from 0 to over 2%, reaching maximum values in A horizons, while TN values were very low in all the samples. The TOC/TN ratio ranged between 7 and 20, reaching maximum values in the A horizons.

Considering the overall C-STOCK$_{tot}$ of each sector within the profiles (Table 2, Figs. 2, 3 and 4), in P1 the values ranged between 0.7 and over 5 kg m^{-2}, reaching minimum and maximum values in sector C and A respectively; in the profile P2 the values spanned from 1.12 to approx. 3 kg m^{-2} reaching minimum values in sector D and maximum in sector F; the C-STOCK$_{tot}$ of P3 reached the minimum value of 2.17 kg m^{-2} in sector K and a maximum of 3.30 in kg m^{-2} in the sector I.

3.3 Geophysical investigation

Results obtained from the long ERT line (ERT3 in Fig. 5a) provided a non-homogeneous electrical resistivity distribution in the plateau bedrock. The deepest values (6-8 kΩ m in the line center below

280 5-m depth, yellow in Fig. 5a) were interpreted as representative of compact bedrock. Higher

281 resistivities (>8 kΩ m, green in Fig. 5a) were depicted at shallower depths, reaching values of 50

282 kΩ m in proximity of the fractured overhanging rock cliff delimiting the plateau eastern edge.

283 These values were related to variable fracturing conditions of the shallow bedrock, increasing

284 towards E and NE. An isolated high-resistivity area (> 75 kΩ m) was found at approx. 2 m depth

285 towards the E-NE section of the ERT3 (Fig. 5a).

286 Above the fractured bedrock, all the short ERT lines revealed the presence of a distinct and

287 discontinuous layer with variable thickness under the stony cover, with resistivity values lower than

288 6 kΩ m (orange to red in Fig. 5, b to d). Separated measurements acquired on an uncovered soil

289 outcrop showed resistivity values in the range 2.9-4.2 kΩ m, with an average of 3.6 kΩ m over 24

290 tests with different array spacing and electrode configuration. Consequently, this shallow layer was

291 interpreted as representative of the soil presence under the periglacial cover.

292 The GPR profiles depicted a complex stratigraphy in the first meters of depth. Exemplificative

293 results are illustrated in Fig. 6 for the GPR profiles acquired along the ERT lines of Fig. 5.

294 Processed radargrams were visually interpreted as shown in Fig. 6a. In the shallowest part of each

295 section, GPR reflections appear as laterally continuous, smooth and sub-horizontal, likely due to the

296 soil presence (s in Fig. 6a). Below this layer, intricate patterns of discontinuous GPR reflections are

297 conversely present, more steeply dipping in different directions. This layer (t in Fig. 6a) possibly

298 corresponds to the transition between soil and bedrock. The chaotic arrangement of soil material

299 and debris resulting from the fractured bedrock may have generated this complex GPR response. At

300 depths higher than 1 m, GPR reflections show again a more homogeneous lateral continuity,

301 possibly indicating the bedrock presence (b in Fig. 6a).

302 Given the difficulty and subjectivity in manually picking the soil bottom basis from GPR sections

303 (Fig. 6, b, d and f), ERT results (Fig. 5) were transformed in total gradient sections of electrical

304 resistivities. The gradient maxima in each section were then automatically picked and interpreted as

305 objective markers of the presence of a sharp vertical and lateral contrast between soil and

surrounding materials and consequently used to estimate the average soil thickness in the plateau. Results are shown in Fig. 6 (c, e and g) in comparison with manual picking performed on GPR sections. Electrical resistivity gradient maxima generally fall within the transition layer (Fig. 6a) depicted in GPR results, providing a rough estimate of the soil-substrate interface.

The soil presence was detected by both geophysical methods within the first meter of depth of all the investigated lines.

3.4 Ground temperature conditions (BTS and GT)

The BTS measurements highlighted a thermal difference between the northern and the southern side of the plateau. Colder ground surface temperatures (often below -2/-3 °C) in the southern portion of the plateau gradually became warmer (generally above -2/-1 °C) towards the northern zone, where only few spots highlighted temperature below -2/-3 °C (Fig. 7a). In additions, a clear correspondence between a cold BTS spot and a high resistivity body detected by the long ERT3 was found (Fig. 7a). Regarding the borehole, maximum GTs reached decisively positive values at all depths during the investigated period (Fig. 7b).

4 Discussion

4.1 Soil properties and carbon stocks

The opening of trenches revealed the unexpected presence of complex and well-developed soils (Umbrisols) under the stony cover, with convolutions and inclusions of different materials, as a result of intense cryoturbation processes as described by Bockheim and Tarnocai (1998) in permafrost-affected soils. Despite the strong geomorphic activity characterizing this periglacial area, the observed soils were extremely well developed, particularly inside periglacial landforms (blockfields and blockstreams). Considering the remarkable thickness of A horizons (up to 60 cm), these soils are considerably more developed than the surrounding soils with or without vegetation,

331 at similar or lower elevation, where weakly developed and shallow Skeletic Regosols, Cambisols or

332 Umbrisols (e.g. Magnani et al., 2017) with thinner A horizon (up to 25-30 cm) were common.

333 Nevertheless, the textural class as well as the pH values were comparable to those found in the

334 surrounding soils under snowbed vegetation (e.g. Magnani et al., 2017). In the Italian Alps, very

335 few works reported soils with C-rich A horizons at high elevation (around 3000 m a.s.l.), for

336 instance Baroni and Orombelli (1996) describe Inceptisols with C-rich A horizons at the Tisa Pass

337 (~ 3200 m a.s.l, Eastern Alps, close to the Italian-Austrian border), although thinner and less

338 developed compared to our soils.

339 Considering the absence of a significant vegetation cover on the plateau and the high elevation, the

340 estimated total carbon stock for each sector was surprisingly high. Overall, the carbon stocks were

341 comparable to the ones reported for high-elevation, cryoturbated soils in the Aosta Valley, although

342 generally covered by alpine tundra, for which values around 2-3 kg m^{-2} (D'Amico et al., still

343 unpublished) were calculated. The values were also in the range reported for other vegetated soils in

344 Alpine tundra ecosystems (Bockheim and Munroe, 2014). Moreover, our results, in particular from

345 soil profile P1, despite the lack of vegetation, were also in the normal range of carbon stock values

346 from moderately developed forest or heath soils in the Aosta Valley, such as Entic Podzols

347 (D'Amico et al., 2020), and to those reported by Chiti et al. (2012) for forest ecosystems in Spain,

348 for mountain boreal forests in North America (Hoffmann et al., 2014) or for mountain soils in the

349 Veneto region (North-East Italian Alps) (Garlato et al., 2009).

350

4.2 Soil distribution, depth and subsurface morphology of the plateau

352 Geophysical investigations confirmed the widespread presence of soils on the whole plateau.

353 Considering the soil texture, the measured electrical resistivity values (up to 6 kΩ m) may appear

354 unusually high for field tests carried out in moist (but unsaturated) conditions on these materials.

355 Since the proportion of minerals having relevant surface conductivity was found to be almost

356   negligible (i.e. illite and chlorite are less than 1% of the total solid matrix), a rough check on the

357   expected soil electrical resistivity ρ_S can be performed following Archie's law (Archie, 1942):

358    $$\rho_S = a \, \frac{\rho_w}{\varphi^m S^k} \tag{4}$$

359   where ρ_w is pore water resistivity (around 100 Ω m, i.e. moisture mainly due to precipitation and

360   shallow seepage), a=1 and m=1.4 are Archie's coefficients for non-consolidated sediments (Archie,

361   1942; Friedman, 2005), φ is the soil porosity (0.5 to 0.6), S is the degree of water saturation and k

362   coefficient can be assumed equal to 2 for S>0.1. Applying Equation 4, retrieved ρ_S values are in the

363   range 1.3-6.5 kΩ m for S between 0.2 and 0.4, thus additionally confirming the obtained electrical

364   resistivity values.

365   Thanks to the electrical resistivity gradient maxima analyses, the soil-substrate interface was

366   recognized at depths ranging from 26 to 88 cm, for an average of 47 cm over the five short ERT

367   lines. In general, higher depths (and soil thicknesses) were identified in the eastern part of the

368   plateau (ERT2, ERT5 in Fig. 1a), close to the chair lift station, in presence of a more fractured

369   underlying bedrock and below a particularly coarse stone cover. By contrast, the lowest depths were

370   found in the grassy area on the northern side of the plateau, where periglacial

371   blockfields/blockstreams are absent (ERT6 in Fig. 1a). A decrease in soil thickness was also

372   observed close to the rock outcrops present in the plateau. Even if ERT surveys had lower vertical

373   resolution with respect to GPR profiles, soil depth and thickness estimations from electrical

374   resistivity gradient maxima were straightforward and provided a less subjective estimation in these

375   complex subsurface settings.

376   Regarding the potential permafrost presence and distribution, relatively low electrical resistivity

377   values pointed towards the absence of relevant bodies of permafrost in the investigated area (e.g.

378   Kneisel, 2006), also considering the lithology of the bedrock and its fracturing conditions. This is in

379   agreement with the BTS values, which indicated higher likelihood of permafrost presence in the

380   southern portion of the plateau, while in the northern portion (where we performed our

381   investigations) generally warmer values suggested only the potential presence of sporadic

permafrost (cf., Julián and Chueca, 2007). Interestingly, a correspondence between a cold BTS spot

and a high resistivity body was found. In this spot, we hypothesize the presence of a body of

isolated permafrost, which is in agreement with its local setting. Further confirmation of the current

mostly permafrost-free conditions of the area derived from the GT data, which evidenced the

absence of permafrost at all depths at the borehole site and relatively warm winter temperatures.

Considering the remarkable thickness of the soil layer (particularly where periglacial features are

thicker) and its general wide distribution, we assume that the overall C-stock of the plateau may be

higher. In particular, the southern and south-western portions of the plateau (impossible to

investigate except by means of heavy machinery) are covered by a particularly coarse and thick

block cover, which resembles the eastern part where the soil thickness and C stocks are larger. In

this area, like in the one overlying the high-resistivity body along the ERT3, the coarse stones thus

protect soil C and permafrost conditions at depth as well.

5 Conclusion and perspectives

During the operational activities for a new chair lift construction at the Stolenberg Plateau, the

opening of soil trenches revealed, unexpectedly, the presence of extremely well-developed soils

under a thick stony cover consisting of periglacial blockfields and blockstreams. These soils,

classified as Umbrisol, were characterized by surprisingly high C stocks, comparable to alpine

tundra or even forest soils, despite the lack of vegetation and the presence of the stony cover. The

application of non-invasive geophysical methods revealed that these hidden soils were widespread

on the plateau under the stony cover, with a mean thickness of around 50 cm, that generally

increase (up to ca. 90 cm) where the periglacial blockfields/blockstreams were thickest.

These C-rich soils, without vegetation and hidden inside periglacial landforms, may represent a

unique pedoenvironment suggesting new perspective on the actual C stocks in high-elevation

environment, which are probably underestimated. Since the origin of these C-rich soils inside

blockstreams and blockfields is apparently in contrast with present day condition, these findings

may be of great relevance for unravelling the history of the high-elevation landscape of the Monte Rosa area. For instance, if these soils represent buried paleosols below moving stone layers, they might retain information about past climate. Alternatively, in order to explain the high organic matter content below the stone cover considering recent conditions, it may be argued that decomposition rates are extremely low as a result of the cooling effect of the stone cover. To clear up those unresolved questions, a more precise characterization of the organic matter, its age and plant remains has to be performed by further studies in the area.

Acknowledgements

References

Alberto, W., Palomba, M., Perotti, L., 2018. SMART GROUND project test-sites topographic and morphologic characterization: Instruments and methodologies. Rendiconti Online Società Geologica Italiana 46, 107–114. https://doi.org/10.3301/ROL.2018.60

Allred B.J., Daniels J.J., Ehsani M.R., 2008. Handbook of Agricultural Geophysics. CRC Press Taylor Francis Group, Boca Raton. https://doi.org/10.1201/9781420019353

Andre F., van Leeuwen C., Saussez S., van Durmen R., Bogaert P., Moghadas D., de Resseguier L., Delvaux B., Vereecken H.; Lambot S., 2012. High-resolution imaging of a vineyard in south of France using ground penetrating radar, electromagnetic induction and electrical resistivity tomography. Journal of Applied Geophysics, 78, 113–122. https://doi.org/10.1016/j.jappgeo.2011.08.002

Archie, G.E., 1942. The electrical resistivity log as an aid in determining some reservoir characteristics. Trans. Am. Inst. Mech. Eng. 146, 54–67. https://doi.org/10.2118/942054-G

Arteaga, G.Á., Calderón, N.G., Krasilnikov, P.V., Sedov, S.N., Targulian, V.O., Rosas, N.V., 2008. Soil altitudinal sequence on base-poor parent material in a montane cloud forest in Sierra Juárez, Southern Mexico. Geoderma 144, 593–612. https://doi.org/10.1016/j.geoderma.2008.01.025

Ballantyne, C.K., Matthews, J.A., 1982. The development of sorted circles on recently deglaciated terrain, Jotunheimen, Norway. Arctic and Alpine Research 14, 341–354. https://doi.org/10.1080/00040851.1982.12004316

Ballantyne, C. K. (2010). A general model of autochthonous blockfield evolution. Permafrost and Periglacial Processes, 21(4), 289-300. https://doi.org/10.1002/ppp.700

Baroni, C., Orombelli, G., 1996. The Alpine "Iceman" and Holocene Climatic Change. Quat. res. 46, 78–83. https://doi.org/10.1006/qres.1996.0046

Batjes, N.H., 1996. Total carbon and nitrogen in the soils of the world. Eur J Soil Science 47, 151–163. https://doi.org/10.1111/j.1365-2389.1996.tb01386.x

Birchak, J.R., Gardner, C.G., Hipp, J.E., and Victor, J.M., 1974. High dielectric constant microwave probes for sensing soil moisture: Proc. IEEE, 62, 93-98. DOI: 10.1109/PROC.1974.9388

Biskaborn, B.K., Smith, S.L., Noetzli, J., Matthes, H., Vieira, G., Streletskiy, D.A., Schoeneich, P., Romanovsky, V.E., Lewkowicz, A.G., Abramov, A., Allard, M., Boike, J., Cable, W.L., Christiansen, H.H., Delaloye, R., Diekmann, B., Drozdov, D., Etzelmüller, B., Grosse, G., Guglielmin, M., Ingeman-Nielsen, T., Isaksen, K., Ishikawa, M., Johansson, M., Johannsson, H., Joo, A., Kaverin, D., Kholodov, A., Konstantinov, P., Kröger, T., Lambiel, C., Lanckman, J.-P., Luo, D., Malkova, G., Meiklejohn, I., Moskalenko, N., Oliva, M., Phillips, M., Ramos, M., Sannel, A.B.K., Sergeev, D., Seybold, C., Skryabin, P., Vasiliev, A., Wu, Q., Yoshikawa, K., Zheleznyak, M., Lantuit, H., 2019. Permafrost is warming at a global scale. Nat Commun 10, 264. https://doi.org/10.1038/s41467-018-08240-4

Bockheim, J.G., Munroe, J.S., 2014. Organic Carbon Pools and Genesis of Alpine Soils with Permafrost: A Review. Arctic, Antarctic, and Alpine Research 46, 987–1006. https://doi.org/10.1657/1938-4246-46.4.987

Bockheim, J.G., Tarnocai, C., 1998. Recognition of cryoturbation for classifying permafrost-affected soils. Geoderma 81, 281–293. https://doi.org/10.1016/S0016-7061(97)00115-8

Bojko, O., Kabala, C., 2017. Organic carbon pools in mountain soils — Sources of variability and predicted changes in relation to climate and land use changes. CATENA 149, 209–220. https://doi.org/10.1016/j.catena.2016.09.022

Boone R.D., Grigal D.F., Sollins P., Ahrens R.J., Armstring, D.E., 1999. Soil sampling, preparation, archiving, and quality control. In: Robertson G.P., Coleman D.C., Bledsoe C.S., Sollins P., (eds) Standard soil methods for long-termecological research. Oxford University Press, New York, pp 3–28.

Carrivick, J.L., Smith, M.W., Quincey, D.J., 2016. Structure from Motion in the Geosciences. John Wiley & Sons, Ltd, Chichester, UK. https://doi.org/10.1111/phor.12173

Celi, L., Rosso, F., Freppaz, M., Agnelli, A., Zanini, E., 2010. Soil Organic Matter Characteristics in Sporadic Permafrost-affected Environment (Creux du Van, Switzerland). Arctic, Antarctic, and Alpine Research 42, 1–8. https://doi.org/10.1657/1938-4246-42.1.1

472   Chiti, T., Díaz-Pinés, E., Rubio, A., 2012. Soil organic carbon stocks of conifers, broadleaf and evergreen
473   broadleaf forests of Spain. Biology and Fertility of Soils, 48(7), 817-826. DOI 10.1007/s00374-012-
474   0676-3

475   Colombo, N., Sambuelli L., Comina C., Colombero C., Giardino M., Gruber, S., Viviano, G., Vittori Antisari, L.,
476   Salerno, F., 2018. Mechanisms linking active rock glaciers and impounded surface water formation in
477   high-mountain areas. Earth Surface Processes and Landforms, 43(2), 417-431. DOI: 10.1002/esp.4257

478   Colombo, N., Salerno, F., Martin, M., Malandrino, M., Giardino, M., Serra, E., Godone, D., Said-Pullicino, D.,
479   Fratianni, S., Paro, L., Tartari, G., Freppaz, M., 2019. Influence of permafrost, rock and ice glaciers on
480   chemistry of high-elevation ponds (NW Italian Alps). Science of The Total Environment, 685, 886-901.
481   https://doi.org/10.1016/j.scitotenv.2019.06.233

482   D'Amico, M., Gorra, R., Freppaz, M., 2015. Small-scale variability of soil properties and soil–vegetation
483   relationships in patterned ground on different lithologies (NW Italian Alps). CATENA 135, 47–58.
484   https://doi.org/10.1016/j.catena.2015.07.005

485   D'Amico, M.E., Pintaldi, E., Catoni, M., Freppaz, M., Bonifacio, E., 2019. Pleistocene periglacial imprinting on
486   polygenetic soils and paleosols in the SW Italian Alps. Catena, 174, 269-284.
487   https://doi.org/10.1016/j.catena.2018.11.019

488   D'Amico, M.E., Pintaldi, E., Sapino, E., Colombo, N., Quaglino, E., Stanchi, S., Navillod, E., Rocco, R., Freppaz,
489   M., 2020. Soil Types of the Aosta Valley (NW Italy). J. Maps.
490   https://doi.org/10.1080/17445647.2020.1821803

491   Daniels, D.J., 2004. Ground Penetrating Radar. 2nd edition. Radar, Sonar, Navigation and Avionics Series 15,
492   Institute of Electrical Engineers, London, UK. DOI: 10.1049/PBRA015E

493   Dong, C., 1999. PowderX: Windows-95 based program for powderX-ray diffraction data processing. J Appl
494   Crystallogr. 32, 838. https://doi.org/10.1107/S0021889899003039

495   Doolittle, J.A., Collins M.E., 1995. Use of soil information to determine application of ground penetrating
496   radar. Journal of Applied Geophysics, 33, 101–108. https://doi.org/10.1016/0926-9851(95)90033-0

497   Egli, M., Mirabella, A., Sartori, G., Zanelli, R., and Bischof, S., 2006: Effect of north and south exposure on
498   weathering rates and clay mineral formation in alpine soils. Catena, 67, 155–174.
499   https://doi.org/10.1016/j.catena.2006.02.010

500   European Commission, 1992. Council Directive 92/43/EEC of 21 May 1992 on the conservation of natural
501   habitats and of wild fauna and flora. Official Journal of the European Union 206, 7–50.
502   http://data.europa.eu/eli/dir/1992/43/oj

503   FAO, 2006. Guidelines for soil description, 4th ed., 2006. Food and Agriculture Organization of the United
504   Nations, Rome. ISBN 92-5-105521-1

505   Freppaz, M., Viglietti, D., Balestrini, R., Lonati, M., Colombo, N., 2019. Climatic and pedoclimatic factors
506   driving C and N dynamics in soil and surface water in the alpine tundra (NW-Italian Alps). NC 34, 67–
507   90. https://doi.org/10.3897/natureconservation.34.30737

508   Friedman, S.P., 2005. Soil properties influencing apparent electrical conductivity: a review. Comput.
509   Electron. Agric. 46, 45–70. https://doi.org/10.1016/j.compag.2004.11.001

510   Garlato, A., Obber, S., Vinci, I., Sartori, G., Manni, G., 2009. Stock attuale di carbonio organico nei suoli di
511   montagna del Veneto. Studi Trentini di Scienze Naturali. Suoli degli ambienti alpini 85, 69–82. ISSN
512   203 5-7 699

513   Gerdol, R., Smiraglia, C., 1990. Correlation between vegetation pattern and microtopography in periglacial
514   areas of the Central Alps. Pirineos 135, 13–28. https://doi.org/10.3989/pirineos.1990.v135.208

515   Goodfellow, B. W., 2007. Relict non-glacial surfaces in formerly glaciated landscapes. Earth-Science
516   Reviews, 80(1-2), 47-73.

517   Hagedorn, F., Mulder, J., Jandl, R., 2010a. Mountain soils under a changing climate and land-use.
518   *Biogeochemistry*, *97*(1), 1-5.   DOI: 10.1007/s10533-009-9386-9

519   Hagedorn, F., Martin, M., Rixen, C. et al., 2010b. Short-term responses of ecosystem carbon fluxes to
520   experimental soil warming at the Swiss alpine treeline. Biogeochemistry 97, 7–19.
521   https://doi.org/0.1007/s 10533-009-9297-9

522   Hoelzle, M., 1992. Permafrost occurrence from BTS measurements and climatic parameters in the Eastern
523   Swiss Alps. Permafrost Periglac 3, 143–147. https://doi.org/10.1002/ppp.3430030212

Hoffmann, U., Hoffmann, T., Johnson, E.A., Kuhn, N.J., 2014. Assessment of variability and uncertainty of soil organic carbon in a mountainous boreal forest (Canadian Rocky Mountains, Alberta). Catena 113, 107–121. https://doi.org/10.1016/j.catena.2013.09.009

Islam A.K.M.E., Lotse, E.G., 1986. Quantitative mineralogical analysis of some Bangladesh soils with X-ray, ion exchange and selective dissolution techniques. Clay Miner. 21, 31–42. https://doi.org/10.1180/claymin.1986.021.1.03

IUSS Working Group WRB, 2015. World Reference Base for Soil Resources 2014, update 2015. International soil classification system for naming soils and creating legends for soil maps. World Soil Resources Reports No. 106. FAO, Rome. E-ISBN 978-92-5-108370-3

Julián, A., Chueca, J., 2007. Permafrost distribution from BTS measurements (Sierra de Telera, central Pyrenees, Spain): assessing the importance of solar radiation in a mid-elevation shaded mountainous area. Permafrost Periglac 18, 137–149. https://doi.org/10.1002/ppp.576

Karte, J., 1983. Periglacial phenomena and their significance as climatic and edaphic indicators. *GeoJournal*, *7*(4), 329-340. https://doi-org.bibliopass.unito.it/10.1007/BF00241455

Kneisel, C., 2006. Assessment of subsurface lithology in mountain environments using 2D resistivity imaging. *Geomorphology*, *80*(1-2), 32-44. https://doi.org/10.1016/j.geomorph.2005.09.012

Kneisel, C., Hauck, C., Fortier, R. and Moorman, B., 2008. Advances in geophysical methods for permafrost investigations. Permafrost Periglac. Process., 19: 157-178. doi:10.1002/ppp.616

Knowles, J.F., Blanken, P.D., Lawrence, C.R., Williams, M.W., 2019. Evidence for non-steady-state carbon emissions from snow-scoured alpine tundra. Nat Commun 10, 1306. https://doi.org/10.1038/s41467-019-09149-2.

Léger, E., Dafflon B., Soom, F., Peterson J., Ulrich C., Hubbard, S., 2017. Quantification of Arctic Soil and Permafrost Properties Using Ground-Penetrating Radar and Electrical Resistivity Tomography Datasets, in IEEE Journal of Selected Topics in Applied Earth Observations and Remote Sensing, vol. 10, no. 10, pp. 4348-4359. doi: 10.1109/JSTARS.2017.2694447

Leifeld, J., Zimmermann, M., Fuhrer, J., Conen, F., 2009. Storage and turnover of carbon in grassland soils along an elevation gradient in the Swiss Alps. Global Change Biology 15, 668–679. https://doi.org/10.1111/j.1365-2486.2008.01782.x

Leopold, M., Voelkel, J., Dethier, D., Williams, M., & Caine, N., 2010. Mountain permafrost—a valid archive to study climate change? Examples from the Rocky Mountains Front Range of Colorado, USA. Nova Acta Leopoldina, 112(384), 281-289.

Magnani, A., Viglietti, D., Godone, D., Williams, M.W., Balestrini, R., Freppaz, M., 2017. Interannual Variability of Soil N and C Forms in Response to Snow—Cover duration and Pedoclimatic Conditions in Alpine Tundra, Northwest Italy. Arctic, Antarctic, and Alpine Research 49, 227–242. https://doi.org/10.1657/AAAR0016-037

Mattirolo, E., Novarese, V., Franchi, S., Stella, A., 1951. Carta Geologica D'Italia 1:100000, foglio 29. Istituto Geografico Militare. Firenze, Italy

McClymont, A. F., Hayashi, M., Bentley, L. R., Muir, D., Ernst, E., 2010. Groundwater flow and storage within an alpine meadow-talus complex, Hydrol. Earth Syst. Sci., 14, 859–872, https://doi.org/10.5194/hess-14-859-2010.

Mollaret, C., Hilbich, C., Pellet, C., Flores-Orozco, A., Delaloye, R., Hauck, C., 2019. Mountain permafrost degradation documented through a network of permanent electrical resistivity tomography sites. The Cryosphere 13, 2557–2578. https://doi.org/10.5194/tc-13-2557-2019

Moorman, B. J., Robinson, S., Burgess, M. M., 2003. Imaging periglacial conditions with ground-penetrating radar. Permafrost and Periglacial Processes 14 (4), 319-329. https://doi.org/10.1002/ppp.463

Novàkovà, E., Karous, M., Zajiček, A., Karousovà, M., 2013. Evaluation of ground penetrating radar and vertical electrical sounding methods to determine soil horizons and bedrock at the locality Dehtáře. Soil & Water Res., 8 (3), pp. 105-112. https://doi.org/10.17221/6/2012-SWR

Otto, J.C., Sass, O., 2006. Comparing geophysical methods for talus slope investigations in the Turtmann valley (Swiss Alps), Geomorphology, Volume 76, Issues 3–4, 257-272. https://doi.org/10.1016/j.geomorph.2005.11.008.

575   Pellet, C., Hilbich, C., Marmy, A., & Hauck, C., 2016. Soil moisture data for the validation of permafrost
576   models using direct and indirect measurement approaches at three alpine sites. Frontiers in Earth
577   Science, 3, 91. https://doi.org/10.3389/feart.2015.00091

578   Samouelian, A., Cousin, I., Tabbagh, A., Bruand, A., Richard, G., 2005. Electrical resistivity survey in soil
579   science: A review, Soil Tillage Res., 83, 173–193, doi:10.1016/j.still.2004.10.004.

580   Schuur, E.A.G., Abbott, B.W., Bowden, W.B., Brovkin, V., Camill, P., Canadell, J.G., Chanton, J.P., Chapin,
581   F.S., Christensen, T.R., Ciais, P., Crosby, B.T., Czimczik, C.I., Grosse, G., Harden, J., Hayes, D.J.,
582   Hugelius, G., Jastrow, J.D., Jones, J.B., Kleinen, T., Koven, C.D., Krinner, G., Kuhry, P., Lawrence, D.M.,
583   McGuire, A.D., Natali, S.M., O'Donnell, J.A., Ping, C.L., Riley, W.J., Rinke, A., Romanovsky, V.E., Sannel,
584   A.B.K., Schädel, C., Schaefer, K., Sky, J., Subin, Z.M., Tarnocai, C., Turetsky, M.R., Waldrop, M.P.,
585   Walter Anthony, K.M., Wickland, K.P., Wilson, C.J., Zimov, S.A., 2013. Expert assessment of
586   vulnerability of permafrost carbon to climate change. Climatic Change 119, 359–374.
587   https://doi.org/10.1007/s10584-013-0730-7

588   Smith, M.V., Carrivick J.L., Quincey D.J., 2015. Structure from motion photogrammetry. Physical Geography
589   40, 247–275. https://doi.org/10.1177/0309133315615805

590   Stanchi, S., Freppaz, M., Walter, S., & Vanderwegen, L., 2015. Mountain soils and threats. In Understanding
591   Mountain Soils: A Contribution from Mountain Areas to the International Year of Soils 2015; Romeo,
592   R., Vita, A., Manuelli, S., Zanini, E., Freppaz, M., Stanchi, S., Eds.; FAO: Rome, Italy, 2015; pp. 88–90,
593   ISBN 978-92-5-108804-3.

594   Van Reeuwijk, L.P., 2002. Procedures for Soil Analysis. Technical Paper n. 9. ISBN: 90-6672-044-1

595   Van Vliet-Lanoë, B., 2014. Patterned ground and climate Change. In: Podrovsky, O. (Ed.), Permafrost:
596   Distribution, Composition and Impacts on Infrastructure and Ecosystems. Nova Science Publishers,
597   Inc. chap 2 pp.67–106. (Results of the IPEV CRYOCLIM 2004 program).

598   Wharton, R.P., Hazen, G.A., Rau, R.A., Best, D.L., 1980. Electromagnetic propagation logging--advances in
599   technique and interpretation: Soc. Petr. Eng., 55th Annual Technical Conference, Paper 9267.

600   Wilson, P., 2013. Block/Rock streams. In Encyclopedia of Quaternary Science, S.A. Elias, Ed., 3. Elsevier:
601   Amsterdam; 514–522.   DOI: 10.1016/B978-0-444-53643-3.00102-3

602   Zollinger, B., Alewell, C., Kneisel, C., Meusburger, K., Gärtner, H., Brandová, D., Ivy-Ochs, S., Schmidt,
603   M.W.I., Egli, M., 2013. Effect of permafrost on the formation of soil organic carbon pools and their
604   physical–chemical properties in the Eastern Swiss Alps. CATENA 110, 70–85.
605   https://doi.org/10.1016/j.catena.2013.06.010

606
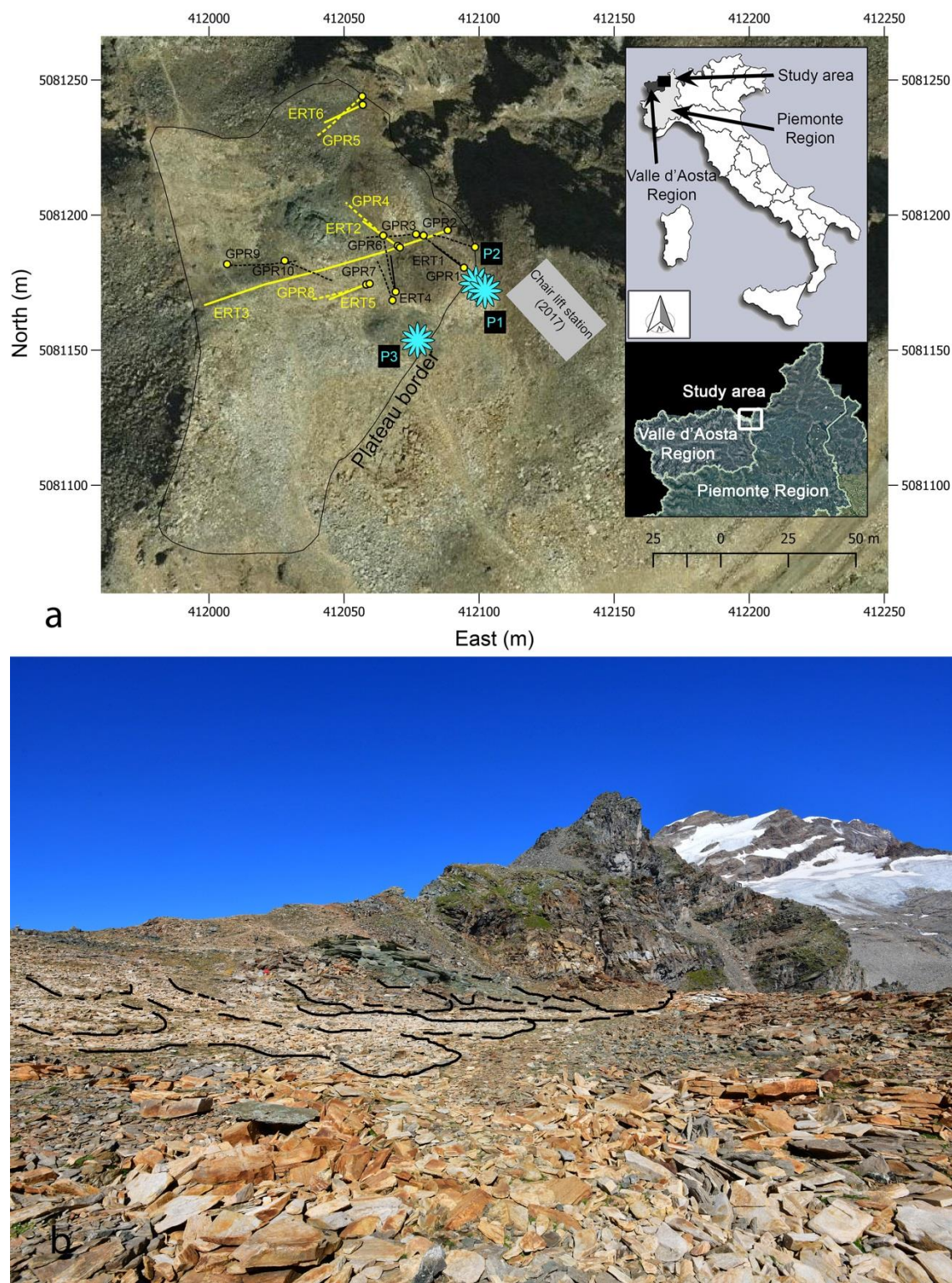
Figures

Figure 1. (a) Location of the study area in the NW Italian Alps (www.pcn.minambiente.it), and overview of the study area (orthoimage Piemonte Region, year 2010); solid and dashed lines indicate ERT and GPR profiles, respectively. Yellow lines indicate the profiles showed and discussed in the manuscript. Yellow circles identify the starting point of each geophysical profile. Cyan polygons indicate the location of the three soil profiles (P1, P2, and P3). (b) View of the plateau (photo by M. D'Amico); dashed lines indicate blockstreams.

614

615
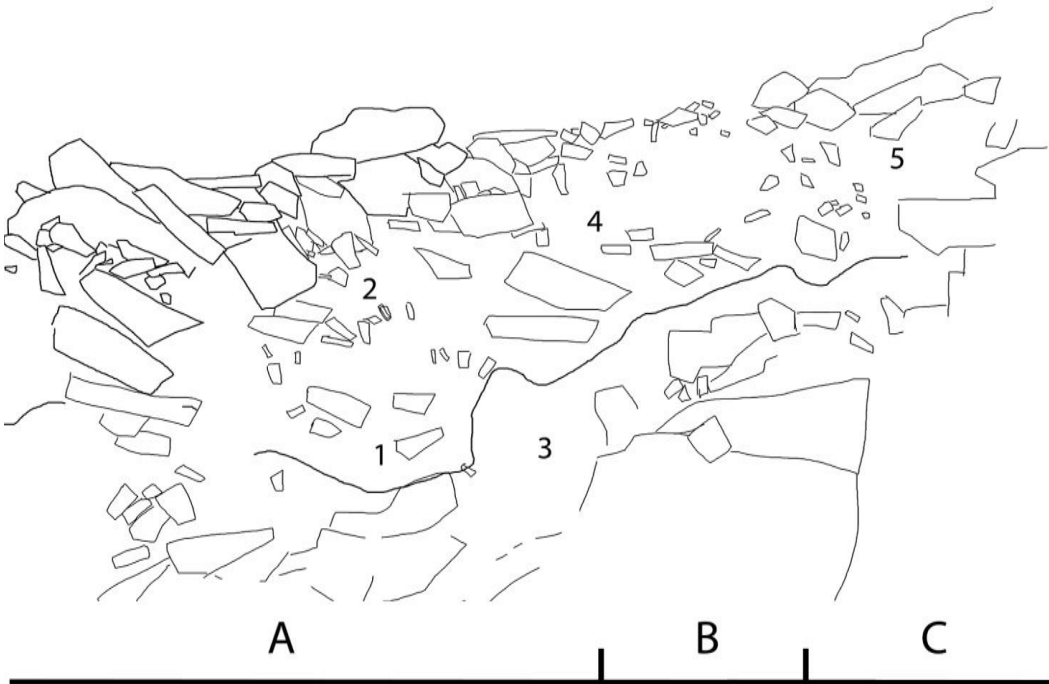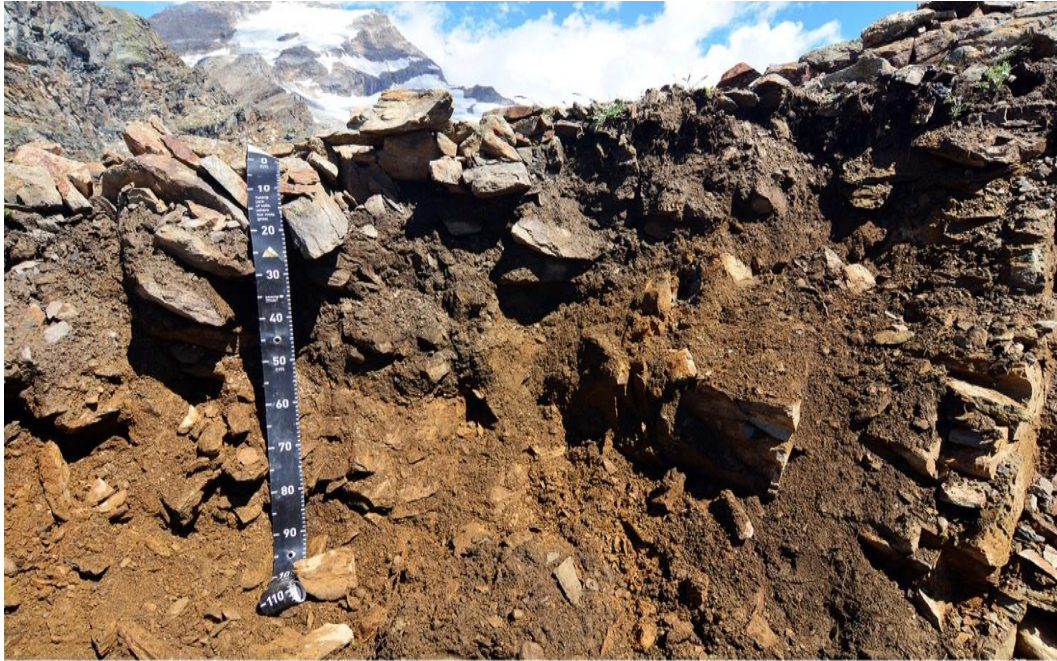
Figure 2. Soil profile P1, with the corresponding scheme (below) reporting sampling points (number), the horizon limits (lines therein) and sectors (letters) in which C-stocks were estimated.

618

619

620

621 **Figure 3. Soil profile P2, with the corresponding scheme (below) reporting sampling points (number), the horizon limits (lines**
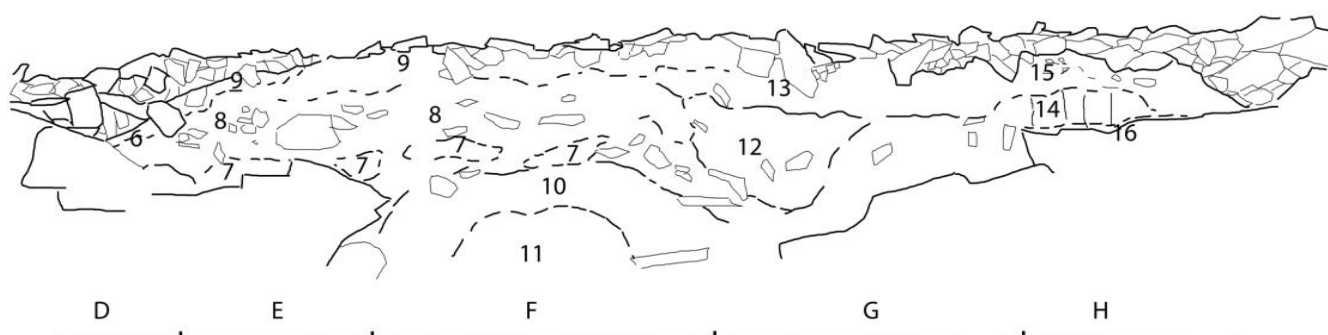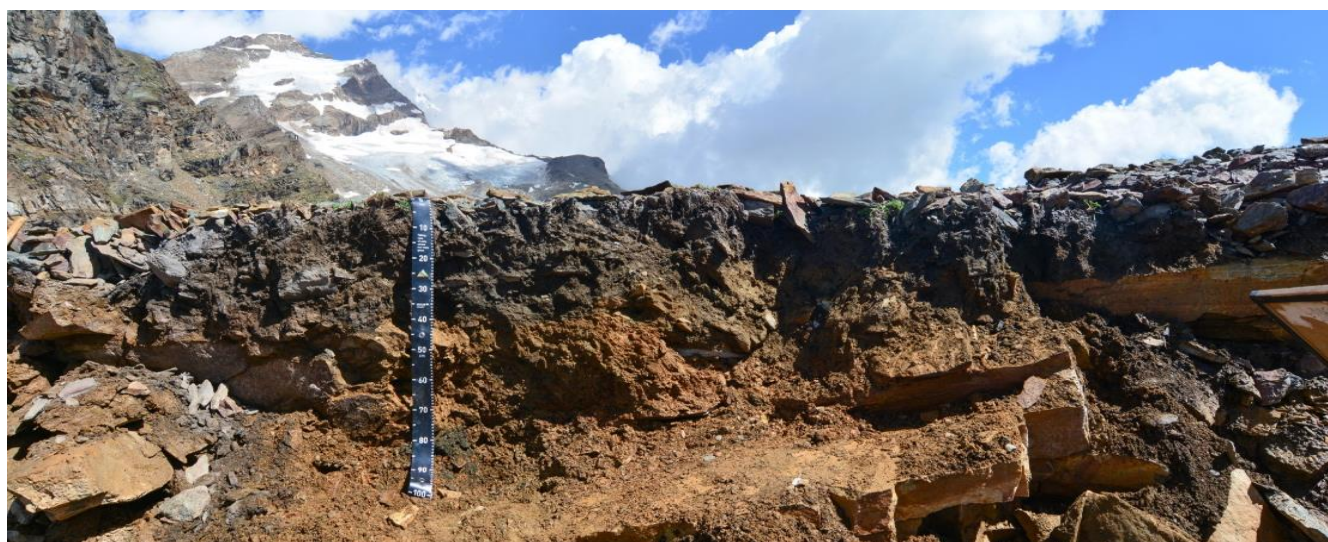622 **therein) and sectors (letters) in which C-stocks were estimated.**

623
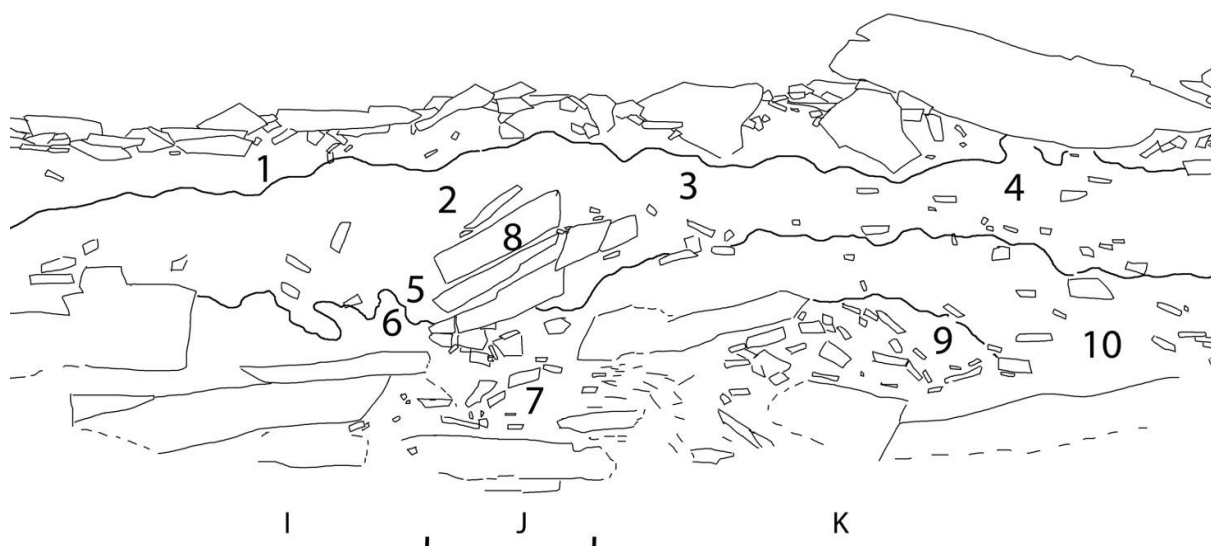
624

625 **Figure 4. Soil profile P3, with the corresponding scheme (below) reporting sampling points (number), the horizon limits (lines**
626 **therein) and sectors (letters I, J, K) in which C-stocks were estimated. Letter "a" indicates blocks dislocated from the rock layer**
627 **evidenced by letters "b" and "c", above a deep fracture (wedge); notches in the meter rule indicate 20 cm intervals.**

628
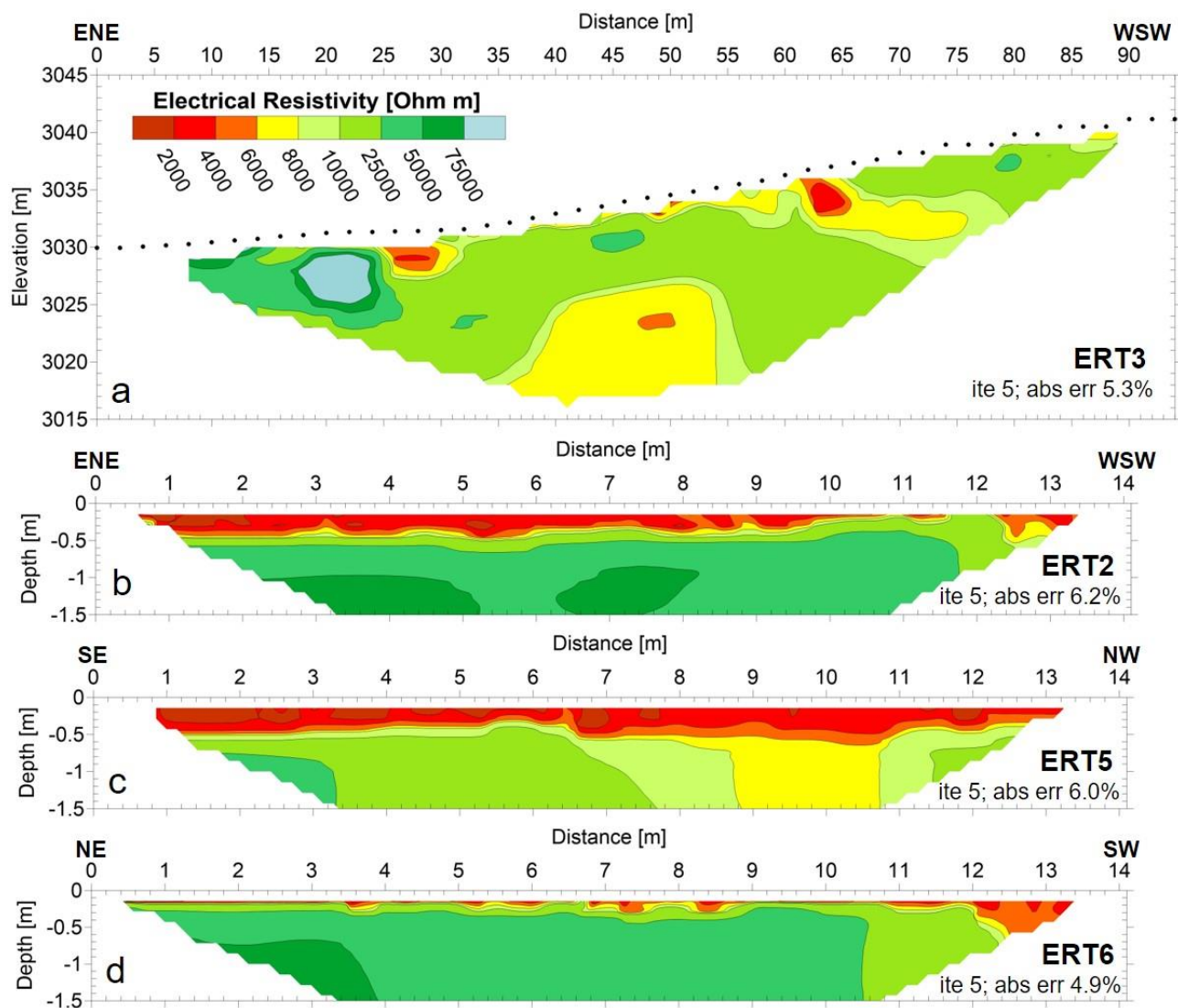
630 **Figure 5. ERT sections: (a) ERT3 (long); (b) ERT2; (c) ERT5; (d) ERT6. The location of the ERT lines is reported in Figure 1. Short**
631 **sections are cut at 1.5-m depth.**

632

633
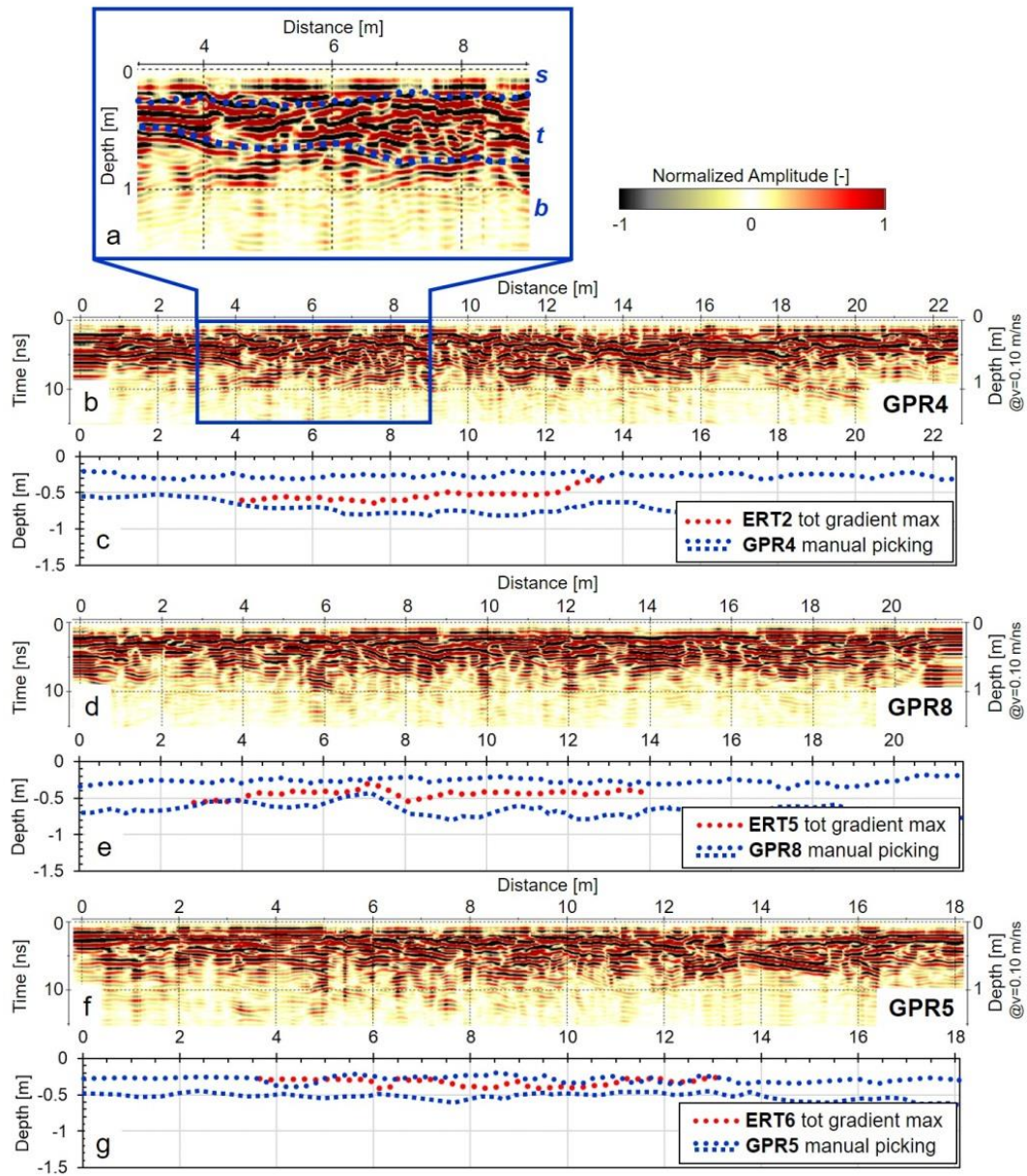
Figure 6. GPR sections. (a) Zoom on GPR4 section with tentative interpretation of the shallow stratigraphy: soil (s), soil-to-bedrock transition (t), bedrock (b). (b, d, f) Processed radargrams for lines GPR4, GPR8, GPR5 (vertical cut at 1.5-m depth). (c, e, g) Soil bottom estimation on the above sections. Comparison between the location of the electrical resistivity gradient maxima computed on the ERT lines of Figure 5 (red dots) and the piking of the different layers on GPR results as shown in Figure 6a (in blue, dotted line: s-t interface, dashed line t-b interface). The location of the GPR profiles is reported in Figure 1.

639
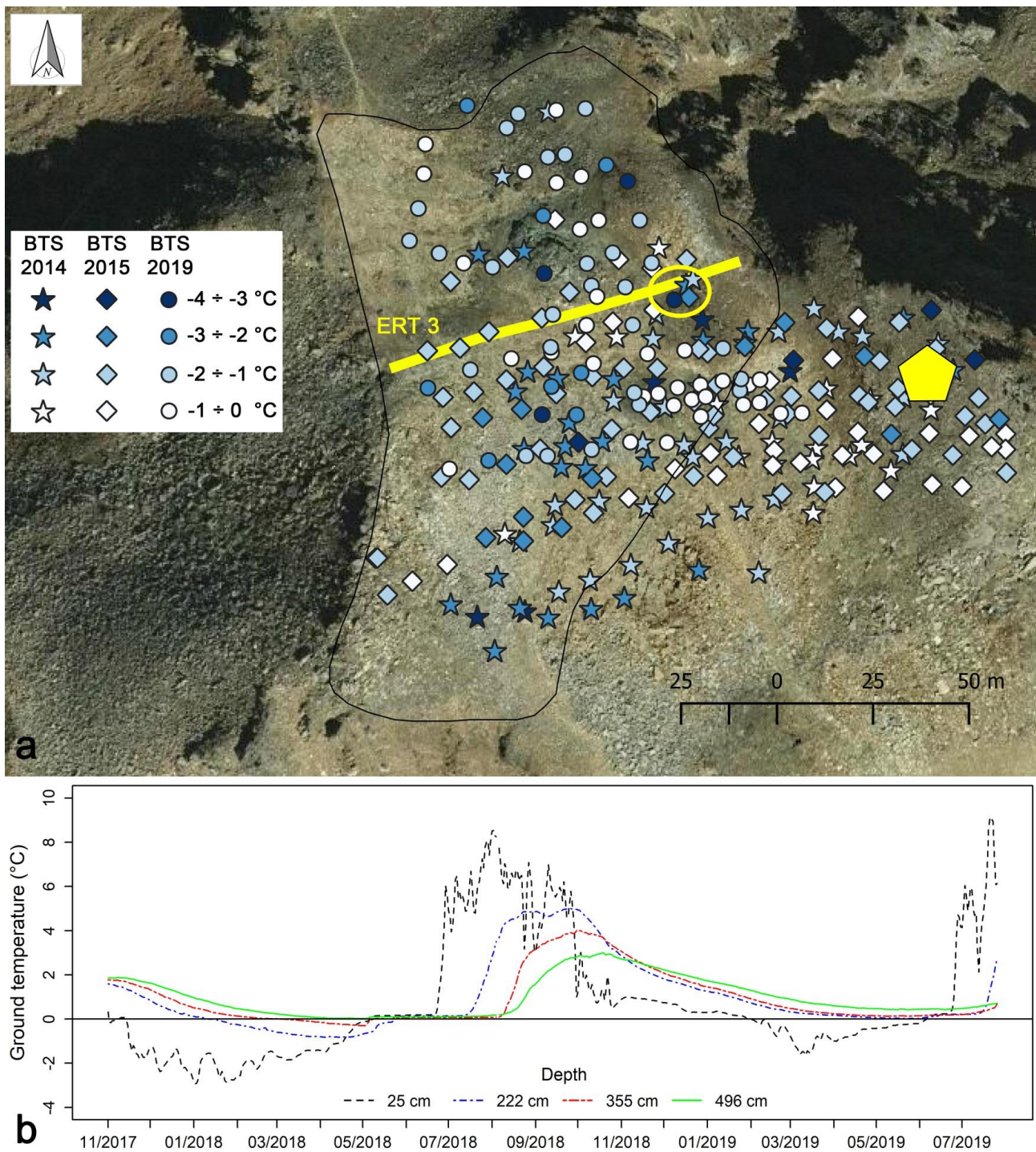
Figure 7. (a) Location and bottom temperatures of the snow cover (BTS) measurements in 2014, 2015, and 2019. Yellow line represents the ERT3; yellow oval indicates the area of correspondence between a cold spot and the high resistivity body detected by the ERT3; yellow polygon indicates the borehole location for the measurement of ground temperature (GT). (b) GT values measured in the 5-m deep borehole of the station managed by Arpa Piemonte in the northern side of the plateau.

Tables

Sample number	Horizon	Munsel colour, moist	Stone fragments (%)	Clay (%)	Silt (%)	Sand (%)	Textural class	Structure	pH	TOC (%)	TN (%)	TOC/TN	BD (kg m^{-3})	TH (m)	VF	C-STOCK (kg m^{-2})
P1
1	A2	10YR 3/2	30	2.8	14.5	82.7	LS	SB	4.8	1.90	0.10	20	1000	0.20	0.70	2.66
2	A1	10YR 3/2	30	2.5	14.9	82.5	LS	SB	4.4	1.08	0.08	13	1000	0.30	0.70	2.26
3	BA	10YR 3/3	40	1.6	23.3	75.2	LS	BL	4.8	0.47	0.04	11	1200	0.20	0.60	0.68
4	A1+A2	10YR 3/2	40	2.7	15.3	82.0	LS	GR	4.7	1.20	0.10	11	1000	0.30	0.60	2.17
5	A	10YR 3/2	80	2.7	14.5	82.9	LS	GR	4.4	1.86	0.15	13	1000	0.20	0.20	0.74
P2
6	A	10YR 2/1	30	2.6	20.8	76.5	LS	SB	4.3	0.80	0.08	11	1000	0.20	0.70	1.12
7	A@	10YR 3/2	10	2.3	23.2	74.5	LS	PL/SB	5.6	2.05	0.11	19	1100	0.05	0.90	1.02
8	A2	10YR 3/3	30	1.9	18.3	79.8	LS	SB	4.7	1.10	0.08	14	1000	0.20	0.70	1.53
9	A1	10YR 3/2	70	2.5	12.1	85.4	LS	GR	4.4	1.13	0.11	11	1000	0.10	0.30	0.34
10	BC	10YR 4/4	70	1.4	27.6	71.0	SL	PL/SB	5.3	0.14	BDL	-	1200	0.20	0.30	0.10
11	CB	10YR 5/2	70	1.0	26.3	72.7	LS	SB	5.9	BDL	BDL	-	1200	0.20	0.30	0.00
12	BW	10YR 3/4	60	0.9	25.7	73.4	LS	SB	5.2	0.26	0.03	9	1200	0.20	0.40	0.25
13	A	10YR 3/2	30	4.3	24.1	71.6	SL	BL	4.8	1.09	0.08	14	1000	0.15	0.70	1.15
14	BA	10YR 3/3	50	2.8	29.3	67.9	SL	CO/PR	4.9	1.10	0.07	15	1200	0.20	0.50	1.32
15	A	10YR 3/2	10	3.9	14.0	82.1	LS	GR	4.5	0.71	0.09	8	1000	0.15	0.90	0.96
16	Silt caps	10YR 6/4	10	6.2	41.9	51.9	SL	PL	5.0	0.28	0.03	8	1300	0.03	0.90	0.10
P3
1	A1	10YR 2/1	70	4.3	8.0	87.7	S	GR	4.9	0.56	0.05	12	1000	0.05	0.30	0.08
2	A2	10YR 3/2	5	3.2	15.6	81.2	LS	GR	4.9	0.87	0.05	17	1000	0.28	0.95	2.28
3	A2	10YR 3/2	5	4.2	15.6	80.1	LS	CO	4.9	1.05	0.07	15	1000	0.25	0.95	2.49
4	A2	10YR 3/2	20	4.8	28.2	66.9	SL	CO	4.8	0.76	0.05	14	1000	0.25	0.80	1.51
5	A2	10YR 3/2	0	4.8	20.7	74.4	SL	SG	4.7	1.18	0.07	17	1000	0.05	1.00	0.59
6	Bw	10YR 5/4	20	2.6	31.8	65.5	SL	SB	5.0	0.15	0.02	7	1200	0.25	0.80	0.35

7	BC	10YR 4/3	50	3.4	16.8	79.9	LS	SB	5.2	0.24	0.02	10	1200	0.20	0.50	0.29
8	A2	10YR 3/2	0	2.8	13.7	83.5	LS	GR	4.9	0.81	0.05	17	1000	0.02	1.00	0.16
9	BC	10YR 4/3	70	4.6	19.5	75.9	LS	PL	5.1	0.31	0.03	9	1200	0.20	0.30	0.22
10	Bw	10YR 3/4	40	3.3	19.6	77.1	LS	SB	5.2	0.16	0.02	8	1200	0.30	0.60	0.36

Table 1. Morphological, physical and chemical properties of the soil samples. Textural class: LS=loamy sand; SL=sandy loam. Structure: SB=subangular blocky; BL=blocky; GR=granular; PL=platy; CO=columnar; PR=prismatic; SG=single grain. BDL=below detection limit.

P1			
Sector	**Horizon**	**Sample number**	**C-STOCK$_{tot}$ (kg m^{-2})**
A	A1 A2 BA	2 1 3b	5.18
B	A1+A2 BA	4 3	2.85
C	A	5	0.74
P2			
D	A	6	1.12
E	A1 A2 A@	9 8 7	2.89
F	A1 A2 A@ BC CB	9 8 7 10 11	2.99
G	A Bw BC	13 12 10b	1.50
H	A BA Silt caps	15 14 16	2.38
P3			
I	A1 A2 A2 Bw	1 2 5 6	3.30
J	A1 A2 A2 BC	1 3 8 7	3.02
K	A1 A2 Bw BC	1 4 10 9	2.17

Table 2. Total C-stock of the profiles for each sector.